Geophysical Research Letters

RESEARCH LETTER
10.1029/2020GL087192

Key Points:
- Both the short- and long-wavelength lower hybrid waves are observed inside a current sheet during guide field reconnection
- A theoretical model, based on local geometry, is developed for the dispersion relation of the lower hybrid drift wave
- The short-wavelength lower hybrid waves are capable of generating anomalous drag between electrons and ions

Supporting Information:
- Supporting Information S1

Correspondence to:
J. Yoo,
jyoo@pppl.gov

Citation:
Yoo, J., Ji, J.-Y., Ambat, M. V., Wang, S., Ji, H., Lo, J., et al. (2020). Lower hybrid drift waves during guide field reconnection. *Geophysical Research Letters*, *47*, e2020GL087192. https://doi.org/10.1029/2020GL087192

Received 21 JAN 2020
Accepted 21 OCT 2020
Accepted article online 29 OCT 2020

Lower Hybrid Drift Waves During Guide Field Reconnection

Jongsoo Yoo[1], Jeong-Young Ji[2], M. V. Ambat[3], Shan Wang[4], Hantao Ji[5], Jenson Lo[5], Bowen Li[6], Yang Ren[1], J. Jara-Almonte[4], Li-Jen Chen[1], William Fox[1], Masaaki Yamada[1], Andrew Alt[1], and Aaron Goodman[1]

[1]Princeton Plasma Physics Laboratory, Princeton, NJ, USA, [2]Department of Physics, Utah State University, Logan, UT, USA, [3]Department of Mechanical Engineering, University of Rochester, Rochester, NY, USA, [4]NASA Goddard Space Flight Center, Greenbelt, MD, USA, [5]Department of Astrophysical Sciences, Princeton University, Princeton, NJ, USA, [6]Department of Physics, Harbin Institute of Technology, Harbin, China

Abstract Generation and propagation of lower hybrid drift wave (LHDW) near the electron diffusion region (EDR) during guide field reconnection at the magnetopause is studied with data from the Magnetospheric Multiscale mission and a theoretical model. Inside the current sheet, the electron beta (β_e) determines which type of LHDW is excited. Inside the EDR, where the electron beta is high ($\beta_e \sim 5$), the long-wavelength electromagnetic LHDW is observed propagating obliquely to the local magnetic field. In contrast, the short-wavelength electrostatic LHDW, propagating nearly perpendicular to the magnetic field, is observed slightly away from the EDR, where β_e is small (~0.6). These observed LHDW features are explained by a local theoretical model, including effects from the electron temperature anisotropy, finite electron heat flux, electrostatics, and parallel current. The short-wavelength LHDW is capable of generating significant drag force between electrons and ions.

Plain Language Summary The lower hybrid drift wave (LHDW) is generated inside the current sheet by the electric current perpendicular to the local magnetic field. With data from the Magnetospheric Multiscale (MMS) mission, we confirm that two types of LHDW are excited in the current sheet during magnetic reconnection with guide field, depending on the local plasma parameter, called beta (ratio between the magnetic field pressure and plasma pressure). One is the short-wavelength, quasi-electrostatic LHDW excited just outside the central reconnection site, called the electron diffusion region. The other is the long-wavelength, electromagnetic LHDW excited in the electron diffusion region. A local theoretical model is developed to explain the excitation of both types of the LHDW in the current sheet. Results from the model agree with MMS observations. The short-wavelength LHDW is capable of generating additional friction between electrons and ions, indicating possible importance of this LHDW on reconnection and electron dynamics.

1. Introduction

Magnetic reconnection (Yamada et al., 2010) rapidly releases magnetic energy through topological rearrangement of magnetic field lines. In the diffusion region, where reconnection occurs, there are various sources of free energy for waves and instabilities. In particular, the lower hybrid drift wave (LHDW) has been frequently observed near the diffusion region in both laboratory (e.g., Carter et al., 2001; Ji et al., 2004; Yoo, Yamada, Ji, Jara-Almonte, Myers, & Chen, 2014) and space plasmas (e.g., Chen et al., 2019; Graham et al., 2017; Norgren et al., 2012). The fast-growing, short-wavelength ($k\rho_e \sim 1$; k is the magnitude of the wave vector $\mathbf{k}$; ρ_e is the electron gyroradius), electrostatic LHDW propagating nearly perpendicular to the local magnetic field ($\mathbf{B}_0$) does not exist near the electron diffusion region (EDR) during antiparallel reconnection (Carter et al., 2001; Roytershteyn et al., 2012, 2013) due to the stabilization by the high plasma beta (β) (Davidson et al., 1977). The long-wavelength ($k\sqrt{\rho_e\rho_i} \sim 1$; ρ_i is the ion gyroradius) electromagnetic LHDW propagating obliquely to $\mathbf{B}_0$ is observed in the EDR (Ji et al., 2004; Roytershteyn et al., 2012), but it does not play an important role in fast reconnection under typical magnetosphere conditions (Roytershteyn et al., 2012).

In most cases, reconnection occurs in the presence of a finite guide field, which is a relatively uniform out-of-plane magnetic field component. The presence of the guide field impacts the structure of the diffusion

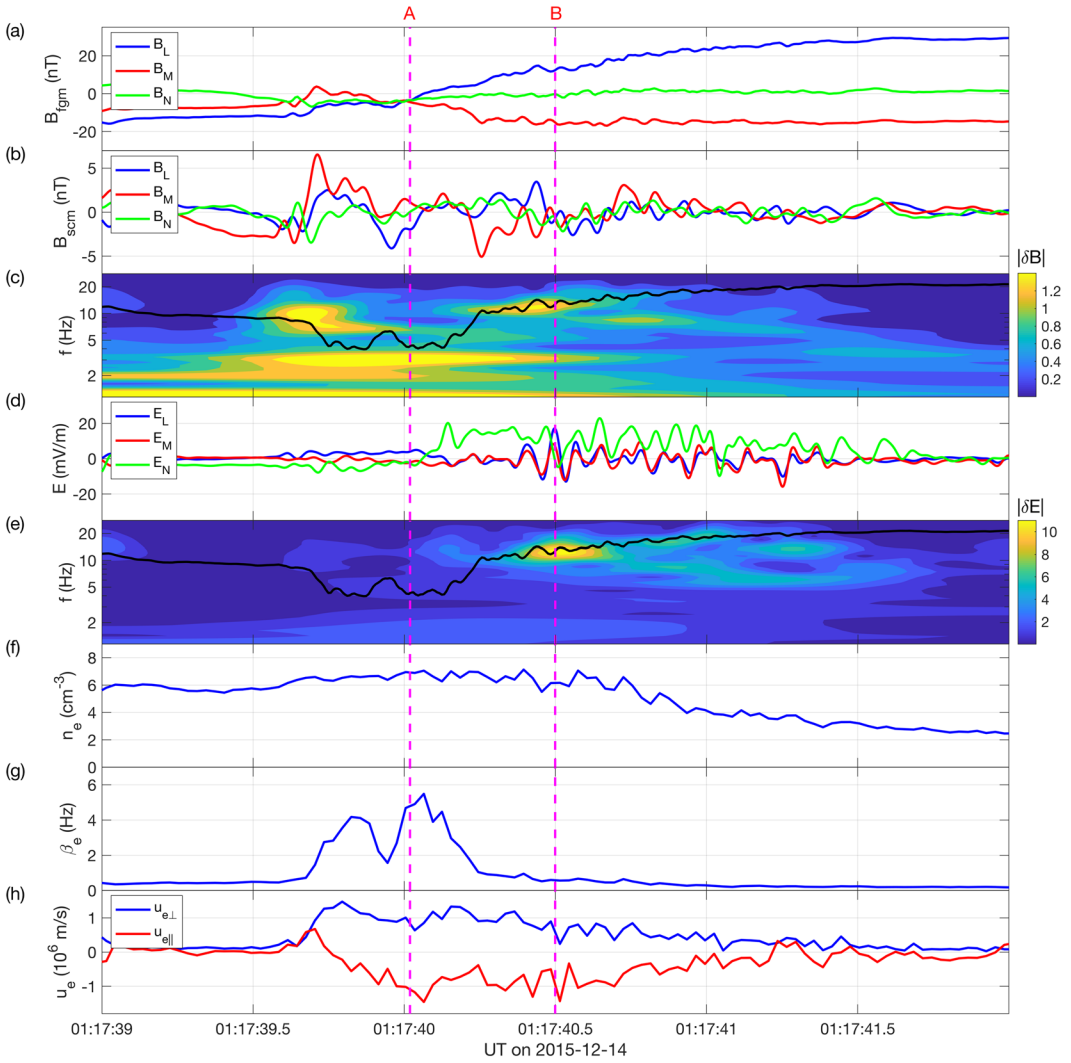

Figure 1. Overview of a magnetopause event with LHDW activity observed by MMS2. Two magenta dashed lines denoted by A and B indicate the time where LHDW stability analysis is performed. Region A represents the EDR, while Region B is slightly outside the EDR. (a) Magnetic field profile measured by FGM. Across the current sheet, there is an average negative B_M component. (b) Magnetic field profile measured by SCM, filtered by a low-pass filter with a cutoff frequency of 40 Hz. (c) Magnetic field spectrogram by the Morlet wavelet. The black line indicates the local lower hybrid frequency, f_{LH}. Fluctuations in the magnetic field persists throughout the current sheet crossing (01:17:39.7–01:17:41.5). In Region A, the fluctuations is below f_{LH}. (d) Electric field profile filtered by the same filter. There are strong fluctuations around Region B. (e) Electric field spectrogram by the wavelet analysis, which demonstrates fluctuations near f_{LH} around Region B. (f) Electron density profile. Density fluctuations exist near B. (g) Profile of β_e. In Region A, β_e is high, while it becomes small around Region B. (h) Profile of the electron flow. Both parallel (red) and perpendicular (blue) components exist throughout the current sheet crossing.

region and electron and ion dynamics (Fox et al., 2017; Pritchett & Coroniti, 2004; Ricci et al., 2004; Tharp et al., 2012). Moreover, the guide field can reduce the value of β in the EDR in such a way that fast-growing, short-wavelength LHDW may exist in the EDR. The short-wavelength LHDW may potentially impact reconnection and electron dynamics in the EDR.

Here, we demonstrate that the short-wavelength LHDW is generated near the EDR by analyzing data from the Magnetospheric Multiscale (MMS) mission. In the analyzed event, there is a moderate guide field ($B_g \sim 0.5B_{rec}$; B_g is the guide field magnitude; B_{rec} is the reconnecting field magnitude). Inside the EDR where the electron beta (β_e) is high (~5), the long-wavelength LHDW is present, while the short-wavelength LHDW is excited slightly away from the EDR where β_e is about 0.6.

Observed LHDW activity is explained by a local theoretical model. This model represents an improvement over a previous model (Ji et al., 2005) due to inclusion of various important effects such as electron temperature anisotropy, finite electron heat flux for the parallel temperature, electrostatics, and parallel electron flow. This new model addresses dynamics of LHDW with an arbitrary angle between $\mathbf{k}$ and $\mathbf{B}_0$ unlike the classical formulation (Davidson et al., 1977). Results from this model agree with measured characteristics of the short-wavelength LHDW where $\mathbf{k}$ is nearly perpendicular to $\mathbf{B}_0$ at $k\rho_e \sim 0.7$. The short-wavelength LHDW produces significant drag force between electrons and ions. In this event, the short-wavelength LHDW exists slightly away from the EDR. However, analysis shows that the short-wavelength LHDW can be exited in the EDR, if there is a guide field enough to decrease β_e in the EDR, potentially affecting electron and reconnection dynamics.

2. Overview of the MMS Event With LHDW

An overview of a magnetopause event, observed by MMS2 on 14 December 2015 (Chen et al., 2017; Ergun et al., 2017), is shown in Figure 1. Here, we use burst-mode data from the fluxgate magnetometer (FGM) (Russell et al., 2016), search coil magnetometer (SCM) (Le Contel et al., 2016), the electric field spin plane (Lindqvist et al., 2016), axial double probes (Ergun et al., 2016), and fast plasma investigation (FPI) (Pollock et al., 2016). Two magenta vertical lines denote two regions where the local dispersion relation for LHDW is calculated. Region A represents the EDR (Chen et al., 2017; Ergun et al., 2017), while Region B is slightly outside the EDR.

The magnetic field profile measured by the FGM is shown in Figure 1a. The transformation matrix from the geocentric solar ecliptic coordinate to the local LMN coordinate system is $(L, M, N) = ([0.095, -0.481, 0.865], [-0.445, -0.811, -0.392], [0.889, -0.346, -0.290])$, which is obtained by a hybrid method (Yoo & Yamada, 2012) using both the minimum variance analysis and timing analysis, with the assumption of the constant thickness (Haaland et al., 2004). The current sheet thickness for this event is about 130 km, which is larger than the ion skin depth d_i in Region B (~90 km). Region A is close to the reversal of the reconnecting field component B_L, while Region B is shifted to the low-density side. Note that there is a density asymmetry across the current sheet with a ratio of about 3, as shown in Figure 1f. Profiles of B_L and the electron flow $\mathbf{u}_e$ in Figure 1h suggest that MMS2 passes through the current sheet between 01:17:39.7 and 01:17:41.5.

The out-of-plane magnetic field component B_M has a negative value on average, indicating there is a guide field for this event. The large perturbation of B_M from 01:17:39.7 to 01:17:40.3 in Figure 1a is due to the bipolar Hall field structure in asymmetric reconnection (Mozer et al., 2008; Pritchett, 2008; Yoo, Yamada, Ji, Jara-Almonte, & Myers, 2014). Excluding this variation, the guide field strength is about 14 nT. Considering the asymmetry (Cassak & Shay, 2007), B_{rec} is about 28 nT. Thus, $B_g \sim 0.5B_{rec}$.

Near Region A, as shown in Figures 1b and 1c, fluctuations in the magnetic field $\mathbf{B}$ exist below the local lower hybrid frequency (f_{LH}, denoted by the black line in (c)). Fluctuations in the electric field $\mathbf{E}$ and electron density n_e are not strong, as shown in Figures 1d and 1f. Around Region B, as shown in Figures 1b–1f, there are fluctuations in $\mathbf{B}$, $\mathbf{E}$, and n_e near f_{LH}. Spectrograms of $\mathbf{B}$ and $\mathbf{E}$, shown in Figures 1c and 1e, indicate that most of the fluctuation power exists near f_{LH}.

Figures 1g and 1h show profiles of β_e and the electron flow vector $\mathbf{u}_e$, respectively. Values of β_e are different in the two regions, about 4.2 in A and 0.6 in B. Values of $\mathbf{u}_e$, in contrast, are similar. Note that both the perpendicular and parallel components of $\mathbf{u}_e$ are significant. The observed features of fluctuations in Region B can be explained by the short-wavelength LHDW. First, the perpendicular electron flow $\mathbf{u}_{e\perp}$ is large. Second, the mode exists when β_e is small. Finally, the frequency of the wave is around f_{LH}.

3. Calculation of the LHDW Dispersion Relation

The geometry of our local model is similar to that of Ji et al. (2005); z is along $\mathbf{B}_0$, and y is along the density gradient direction in the ion rest frame. The wave vector is assumed on the x-z plane with an assumption of negligible k_y. Unlike Ji et al. (2005), the equilibrium electron flow velocity ($\mathbf{u}_{e0}$) has a parallel component (u_{e0z}). Equilibrium temperature is assumed to be uniform, and ion temperature anisotropy is ignored.

The detailed derivation of the dispersion relation is provided in the supporting information. Here, only important improvements over the model in Ji et al. (2005) are discussed. First, for the quasi-electrostatic

nature of the short-wavelength LHDW, the perturbed electron density n_{e1} is independently obtained from the electron continuity equation:

$$(\omega - \mathbf{k}\cdot\mathbf{u}_{e0})n_{e1} = (\mathbf{k}\cdot\mathbf{u}_{e1} - i\epsilon u_{e1y})n_{e0}, \tag{1}$$

where the subscript 1 indicates perturbed quantities while the subscript 0 indicates equilibrium quantities, $\mathbf{u}_{e0}$ is the equilibrium electron flow, $\mathbf{u}_{e1}$ is the perturbed electron flow velocity, n_{e0} is the equilibrium density, and $\epsilon = (dn_{e0}/dy)/n_{e0}$ is the inverse of the density gradient scale. The electron temperature anisotropy is also taken into account; $T_{e0}^{\perp} \neq T_{e0}^{\parallel}$, where $T_{e0}^{\perp}$ and $T_{e0}^{\parallel}$ are the perpendicular and parallel electron equilibrium temperature, respectively.

The perturbed perpendicular electron pressure is assumed to be $p_{e1}^{\perp} \approx n_{e1}T_{e0}^{\perp}$, which means that the perpendicular temperature perturbation is ignored (isothermal limit). This simplification is justifiable because LHDW stability does not depend strongly on the specific form of $p_{e1}^{\perp}$; other terms such as $\mathbf{E}_1$, $\mathbf{u}_{e1}\times\mathbf{B}_0$, and $\mathbf{u}_{e0}\times\mathbf{B}_1$ are more important for the electron momentum balance along the perpendicular direction. Here, $\mathbf{E}_1$ and $\mathbf{B}_1$ are the perturbed electric and magnetic field, respectively. This isothermal limit implies infinite heat flux for the perpendicular temperature. We find that the dispersion relation does not change much even in the limit of the zero heat flux.

For the parallel direction, however, it is important to consider a more rigorous closure for the perturbed parallel electron pressure, $p_{e1}^{\parallel}$. To obtain $p_{e1}^{\parallel}$, we start from the following equation from the Vlasov equation:

$$\frac{\partial p_e^{\parallel}}{\partial t} + \nabla\cdot(\mathbf{u}_e p_e^{\parallel}) + \nabla\cdot\mathbf{q}_e^{\parallel} + 2\frac{\partial u_{ez}}{\partial z}p_e^{\parallel} = 0, \tag{2}$$

where $p_e^{\parallel} = m_e\int(v_z - u_{ez})^2 f_e d\mathbf{v}$, $\mathbf{q}_e^{\parallel} = m_e\int(\mathbf{v}-\mathbf{u}_e)(v_z-u_{ez})^2 f_e d\mathbf{v}$, and $n_e\mathbf{u}_e = \int\mathbf{v}f_e d\mathbf{v}$. Note that $\mathbf{q}_e^{\parallel}$ is the electron heat flux affecting the parallel electron temperature rather than the parallel heat flux.

A closure for $\mathbf{q}_e^{\parallel}$ is required for $p_{e1}^{\parallel}$. The 3 + 1 fluid model (Ji & Joseph, 2018) gives

$$\mathbf{q}_e^{\parallel} = \frac{\hat{z}}{m_e\omega_{ce}}\times\left(p_e^{\parallel}\nabla T_e + T_e\nabla p_e^{\parallel} - \frac{T_e}{2}\nabla\pi_e^{\parallel} - T_e^{\parallel}\nabla p_e^{\perp}\right) + q_{ez}^{\parallel}\hat{z}, \tag{3}$$

where $\pi_e^{\parallel} = 2(p_e^{\parallel} - p_e^{\perp})/3$ and $T_e = (2T_e^{\perp} + T_e^{\parallel})/3$. The derivation of this equation is also given in the supporting information. The closure for $q_{e1z}^{\parallel}$ in the collisionless limit is (Ji & Joseph, 2018)

$$q_{e1z}^{\parallel} = \frac{-i}{\sqrt{\pi}}\frac{k_{\parallel}}{|k_{\parallel}|}2n_0 v_{te}T_{e1}^{\parallel}, \tag{4}$$

where $T_{e1}^{\parallel} = (p_{e1}^{\parallel} - T_{e0}^{\parallel}n_1)/n_0$ is the perturbed parallel temperature and $v_{te} = \sqrt{2T_{e0}/m_e}$ is the electron thermal speed. By linearizing Equation 3, $q_{e1x}^{\parallel}$ becomes

$$q_{e1x}^{\parallel} = -\frac{2}{9}\frac{(T_{e0}^{\parallel} - 4T_{e0}^{\perp})T_{e1}^{\parallel}}{T_{e0}^{\perp} + T_{i0}}n_0 u_{e0x} = r_e^{\parallel}T_{e1}^{\parallel}n_0 u_{e0x}, \tag{5}$$

where $r_e^{\parallel} = 2(4T_{e0}^{\perp} - T_{e0}^{\parallel})/9(T_{e0}^{\perp} + T_{i0})$. With Equations 2, 4, and 5, $p_{e1}^{\parallel}$ is given by

$$p_{e1}^{\parallel} = n_{e1}T_{e0}^{\parallel} + \frac{2k_{\parallel}n_0 T_{e0}^{\parallel}u_{e1z}}{\omega - \mathbf{k}\cdot\mathbf{u}_{e0} - r_e^{\parallel}k_{\perp}u_{e0x} + i(2/\sqrt{\pi})|k_{\parallel}|v_{te}}. \tag{6}$$

With these closures, the electron momentum equation is solved to obtain the perturbed electron current density, $\mathbf{J}_{e1}$. The ion current is given by (Ji et al., 2005)

$$\mathbf{J}_{i1} = -\frac{in_0e^2}{m_i k v_{ti}}\left[Z(\zeta)\mathbf{E}_1 + \frac{Z''(\mathbf{E}_1\cdot\hat{\mathbf{k}})}{2}\hat{\mathbf{k}} - i\left(\frac{\epsilon}{2k}\right)Z''E_{1y}\hat{\mathbf{k}}\right], \tag{7}$$

where m_i is the ion mass, $v_{ti} = \sqrt{2T_{i0}/m_i}$ is the ion thermal speed, $\zeta = \omega/kv_{ti}$, and $Z(\zeta)$ is the plasma dispersion function. With $\mathbf{J}_1 = \mathbf{J}_{e1} + \mathbf{J}_{i1}$, the Maxwell equation without the displacement current $\mathbf{k}\times(\mathbf{k}\times\mathbf{E}_1) = -i\omega\mu_0\mathbf{J}_1$ can be expressed as

$$\begin{pmatrix} D_{xx} & D_{xy} & D_{xz} \\ D_{yx} & D_{yy} & D_{yz} \\ D_{zx} & D_{zy} & D_{zz} \end{pmatrix}\begin{pmatrix} E_{1x} \\ E_{1y} \\ E_{1z} \end{pmatrix} = 0, \tag{8}$$

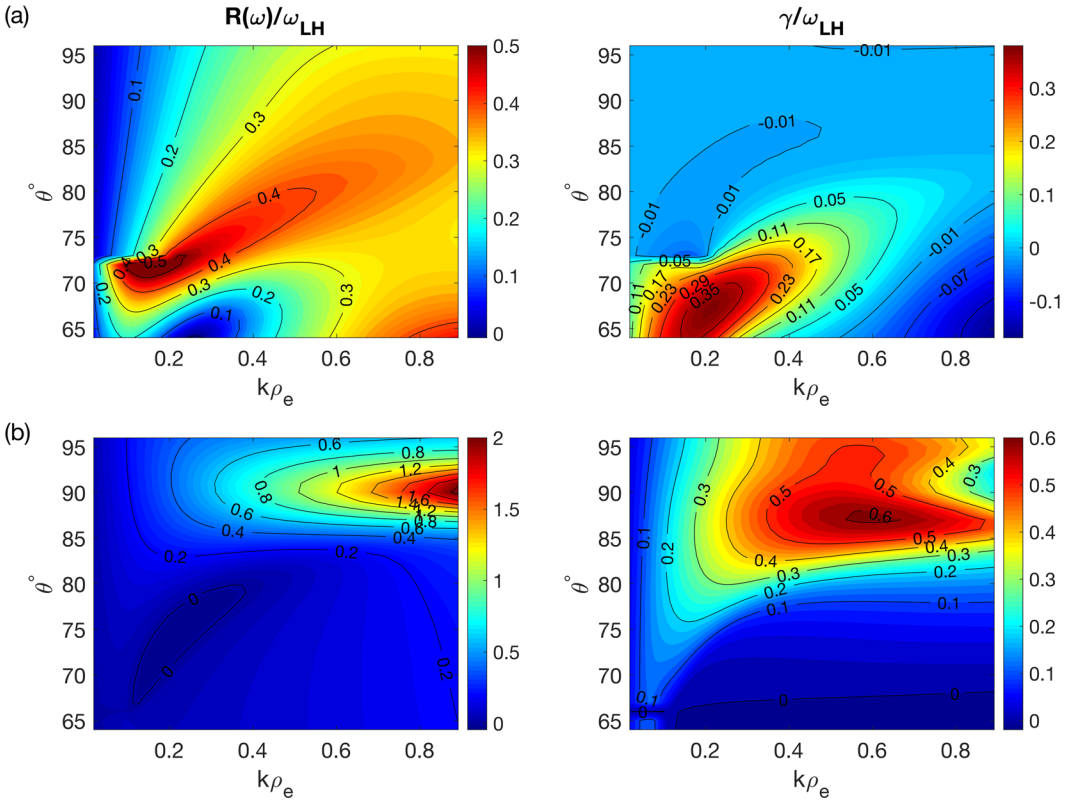

Figure 2. Dispersion relation of LHDW for Region A (panel (a)) and Region B (panel (b)). For each subplot, the left (right) panel shows the contour plot for the real (imaginary) part of the angular frequency normalized by the local lower hybrid frequency ω_{LH} as a function of $k\rho_e$ and θ. Here, ρ_e is the electron gyroradius in Region B even for the axis of panels (a). (a) In Region A, the long-wavelength LHDW ($\theta \sim 70°$ is unstable, while the short-wavelength LHDW is marginally stable ($\gamma \sim 0$) due to high β. (b) In Region B, the short-wavelength LHDW has fast growth rates $\gamma \sim 0.6\omega_{LH}$ with $\Re(\omega) \sim \omega_{LH}$.

with a tensor **D**. The dispersion relation for the wave can be obtained from det **D** = 0. The calculation for each component of **D** is provided in the supporting information.

Dispersion relations are obtained with plasma and field parameters measured in Regions A and B. For Region A, the parameters averaged over 01:17:39.989–01:17:40.049 are $B_0 = 6.5\,\text{nT}$, $n_0 = 6.1\,\text{cm}^{-3}$, $T_{e0}^{\parallel} = 79.5\,\text{eV}$, $T_{e0}^{\perp} = 70.9\,\text{eV}$, $T_{i0} = 395\,\text{eV}$, $u_{e0x} = 17.9V_A$, and $u_{e0z} = -14.1V_A$, where $V_A = 57.7\,\text{km/s}$ is the local Alfvén speed. With these values, $\beta_e = 4.24$ and $f_{LH} = 4.4\,\text{Hz}$. For Region B, the parameters averaged over 01:17:40.469–529 are $B_0 = 19.8\,\text{nT}$, $n_0 = 6.2\,\text{cm}^{-3}$, $T_{e0}^{\parallel} = 122\,\text{eV}$, $T_{e0}^{\perp} = 77.6\,\text{eV}$, $T_{i0} = 402\,\text{eV}$, $u_{e0x} = 2.65V_A$, and $u_{e0z} = -5.07V_A$ with $V_A = 174\,\text{km/s}$, $\beta_e = 0.58$, and $f_{LH} = 12.9\,\text{Hz}$.

The calculated dispersion relation with parameters in Region A is shown in Figure 2a; the left and right panels show, respectively, the real and imaginary parts of the angular frequency as a function of k and θ, which is normalized to the local (angular) lower hybrid frequency, ω_{LH}. Here, θ is the angle between **k** and $\mathbf{B}_0$ (see Figure S1 in the supporting information). In Region A, the short-wavelength LHDW around $\theta = 90°$ is marginally stable despite the strong electron flow. The long-wavelength LHDW around $\theta = 70°$, in contrast, is unstable around $f < 0.5f_{LH}$, which agrees with measurements in Figure 1c.

In Region B, the short-wavelength LHDW has large growth rates with a maximum growth rate of $\gamma_{max} \sim 0.6\omega_{LH}$, as shown in Figure 2b. The frequency near γ_{max} is $\sim 0.8f_{LH}$. The model expects $k_\perp \gg |k_\parallel|$. All of these features are consistent with those of the short-wavelength LHDW (Davidson et al., 1977). The biggest difference between parameters of Regions A and B is β_e, which determines whether the long-wavelength or the short-wavelength LHDW is excited. Thus, in principle, the short-wavelength LHDW can exists inside the EDR if there is a guide field enough to lower β_e.

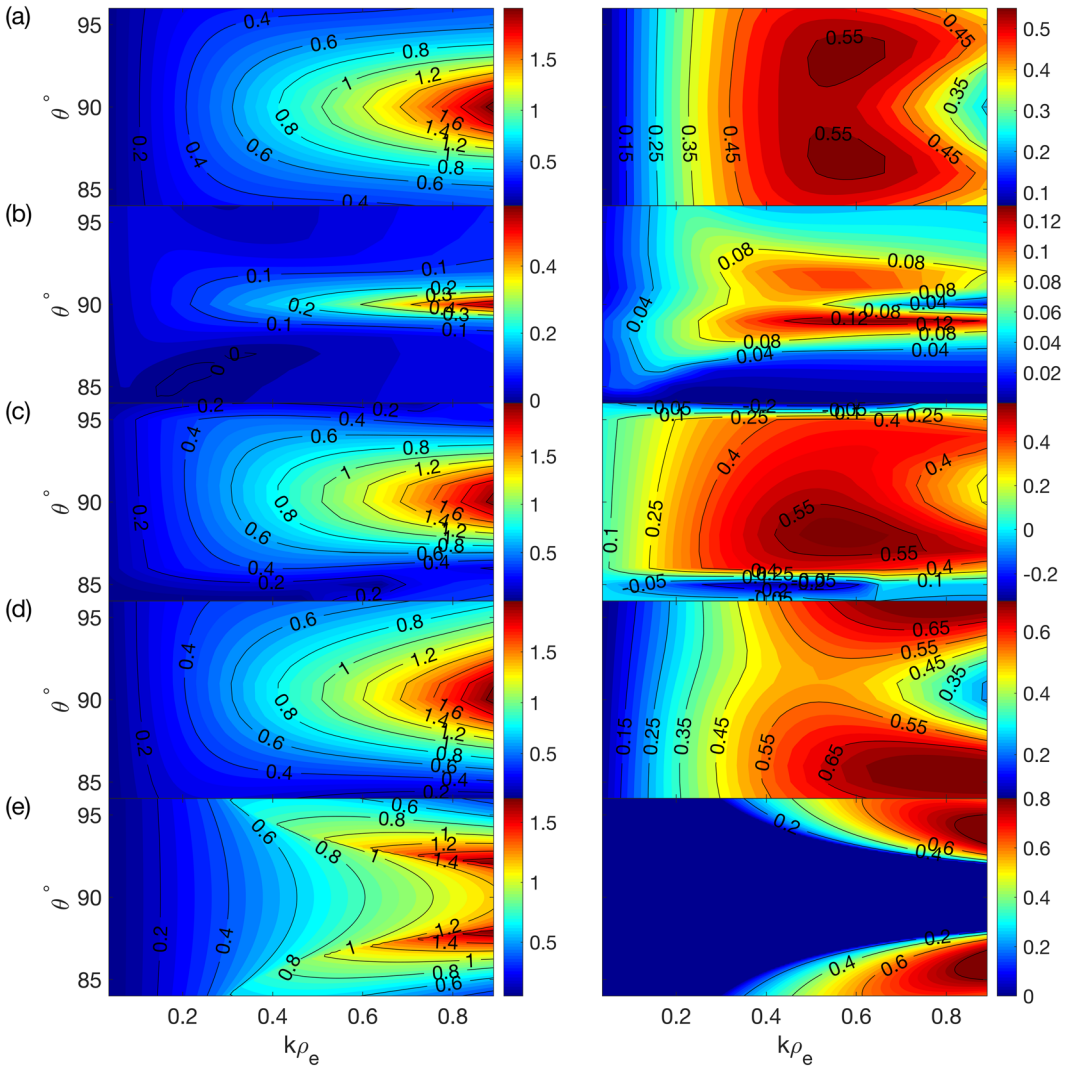

Figure 3. Dispersion relation of LHDW with plasma and field parameters of region. In each subplot, either a key physical parameters or set of assumptions is changed. The reference case is shown in Figure 2b. Note that the range of θ is reduced to focus on the dynamics of the short-wavelength LHDW. Again, for each subplot, the left (right) panel shows the contour plot for the real (imaginary) part of the angular frequency normalized by the local lower hybrid frequency. (a) Dispersion relation with $u_{e0z} = 0$. Without the parallel flow, the dispersion becomes symmetric with respect to $\theta = 90°$, but there is no significant change in γ. (b) Dispersion relation with $u_{e0x} = 0.7V_A$. When the perpendicular flow is reduced, γ becomes much smaller, which indicates u_{e0x} is the free energy source. (c) Dispersion relation with $\mathbf{q}_e^{\parallel} = 0$. The oblique modes are stabilized. (d) Dispersion relation without $T_{e1}^{\parallel}$ ($\mathbf{q}_e^{\parallel} \to \infty$). With the infinite heat flux, γ becomes generally larger especially for more oblique modes, which shifts $\Re(\omega)$ with the maximum γ to about $0.4\omega_{LH}$. (e) Dispersion relation from the previous model by Ji et al. (2005). This model cannot properly address the short-wavelength LHDW, especially around $\theta \sim 90°$.

To understand the dynamics of the short-wavelength LHDW, dispersion relations of LHDW with plasma and field parameters of Region B but with different assumptions are presented in Figure 3. First, the impact from the electron flow velocity on LHDW is studied by artificially reducing each component of $\mathbf{u}_{e0}$. The effect of u_{e0z} on the short-wavelength LHDW is limited. As shown in Figure 3a, there is no significant change in either real or imaginary parts of the angular frequency even when u_{e0z} is reduced to 0. Note that the dispersion function becomes symmetric with respect to $\theta = 90°$ with $u_{e0z} = 0$. The dynamics of LHDW, on the other hand, depends strongly on the perpendicular flow velocity. When the perpendicular velocity is decreased from $2.65V_A$ to $0.7V_A$, γ becomes small, as shown in Figure 3b. If u_{e0x} is reduced below $0.5V_A$, the mode disappears. This indicates that the free energy source for LHDW is the perpendicular current.

To understand the effect of the heat flux ($\mathbf{q}_e^{\parallel}$) on the dispersion, we have tested two limits—no heat flux and infinite heat flux. Without the heat flux, $p_{e1}^{\parallel}$ in Equation 6 becomes

$$p_{e1}^{\parallel} = n_{e1} T_{e0}^{\parallel} + \frac{2k_{\parallel} n_0 T_{e0}^{\parallel} u_{e1z}}{\omega - \mathbf{k}\cdot\mathbf{u}_{e0}}. \tag{9}$$

With the infinite heat flux ($v_{th} \to \infty$), $p_{e1}^{\parallel} = n_{e1} T_{e0}^{\parallel}$, which means $T_{e1}^{\parallel} = 0$ (isothermal limit). Figures 3c and 3d show the dispersion for these two limits. When θ is close to 90°, the results are not affected. For oblique modes, however, the heat flux significantly affects the dispersion relation, especially the growth rate. Without $\mathbf{q}_e^{\parallel}$, oblique modes are quickly stabilized; as shown in Figure 3c, γ becomes negative for $\theta \sim 85°$ or $\theta \sim 96°$. With the infinite heat flux (zero $T_{e1}^{\parallel}$), on the other hand, γ for oblique modes becomes larger than values in Figure 2b, as shown in Figure 3d.

This dependence of γ on $\mathbf{q}_e^{\parallel}$ can be understood by the parallel force balance. The perturbed pressure term, $ik_{\parallel} p_{e1}^{\parallel}$ can be interpreted as a restoring force against the electric field perturbation. The heat flux reduces the temperature perturbation, which means that the restoring force decreases as the heat flux increases. Thus, in the limit of the infinite (zero) heat flux, γ becomes larger (smaller) for oblique modes. For modes around $\theta = 90°$, the impact from the heat flux is negligible, since the perturbed pressure term $ik_{\parallel} p_{e1}^{\parallel}$ becomes small ($k_{\parallel} \to 0$).

Finally, dispersion relation of LHDW from the model by Ji et al. (2005) is presented in Figure 3e for comparison. The previous model does not properly describe the short-wavelength LHDW especially around $\theta = 90°$. This is because the perturbed electron density is set to be the same of that of ions, thereby neglecting electrostatic effects. Moreover, this model overestimates the growth rate of oblique modes since it uses the isothermal closure (infinite heat flux) for the perturbed electron pressure, which is similar to the case in Figure 3d.

4. Comparison Between Theory and Observation

The dispersion relation is crucial for identifying waves and understanding their propagation. If all MMS satellites observed the same wave packet, $\mathbf{k}$ could be estimated directly from the phase difference (Yoo et al., 2018). However, for this event, signals from only MMS2 and MMS4 have correlation, while they are near Region B. Thus, single spacecraft methods such as the singular value decomposition (SVD) analysis (Santolík et al., 2003) should be considered.

The SVD analysis has its own caveat; this method relies on the assumption that there is only one dominant $\mathbf{k}$ for a given frequency. This assumption is not valid for LHDW; as shown in Figure 3b, there are ranges of k and θ that has a positive growth rate for a given frequency. In this case, the estimated $\mathbf{k}$ is a power-weighted average of multiple wave vectors, which underestimates the magnitude of $\mathbf{k}$ (Yoo et al., 2019). The direction of the estimated $\mathbf{k}$, on the other hand, still indicates the average propagation direction.

The wave vector $\mathbf{k}$ is estimated by combining two methods. With the unit vector $\hat{\mathbf{k}}$ from the SVD analysis, the magnitude k is

$$k = \frac{\phi_2 - \phi_4}{\hat{\mathbf{k}}\cdot(\mathbf{r}_2 - \mathbf{r}_4)}, \tag{10}$$

where ϕ_2 and ϕ_4 are the phase of the correlated signal measured by MMS2 and MMS4, while $\mathbf{r}_2$ and $\mathbf{r}_4$ are the location of MMS2 and MMS4, respectively. The phase information comes from the Morlet wavelet transform of E_M (Torrence & Compo, 1998). As shown in Figure 4a, E_M signals from two satellites are correlated in Region B (cyan box).

Figure 4b shows the measured $k\rho_e$ (blue asterisks), compared with theoretical values (solid lines). For theoretical values, the Doppler shift due to the frame difference is considered, which is $\Delta f = \mathbf{u}_i \cdot \mathbf{k}/2\pi$. Here, $\mathbf{u}_i$ is the ion flow velocity in the spacecraft frame ($u_{ix} = 33$ km/s, $u_{iz} = -38$ km/s). At $f = 0.98 f_{LH}$, $k\rho_e = 0.66$, which agrees with the theoretical value with $\theta \sim 87°$. Note that the mode with the highest growth rate exists around $\theta \sim 87°$ and $k\rho_e \sim 0.6$, as shown in Figure 3b.

Figure 4c shows the measured θ (blue asterisks), compared with theoretical values of various k (solid lines). The measurement shows that LHDW propagates almost perpendicular to $\mathbf{B}_0$, which agrees with the

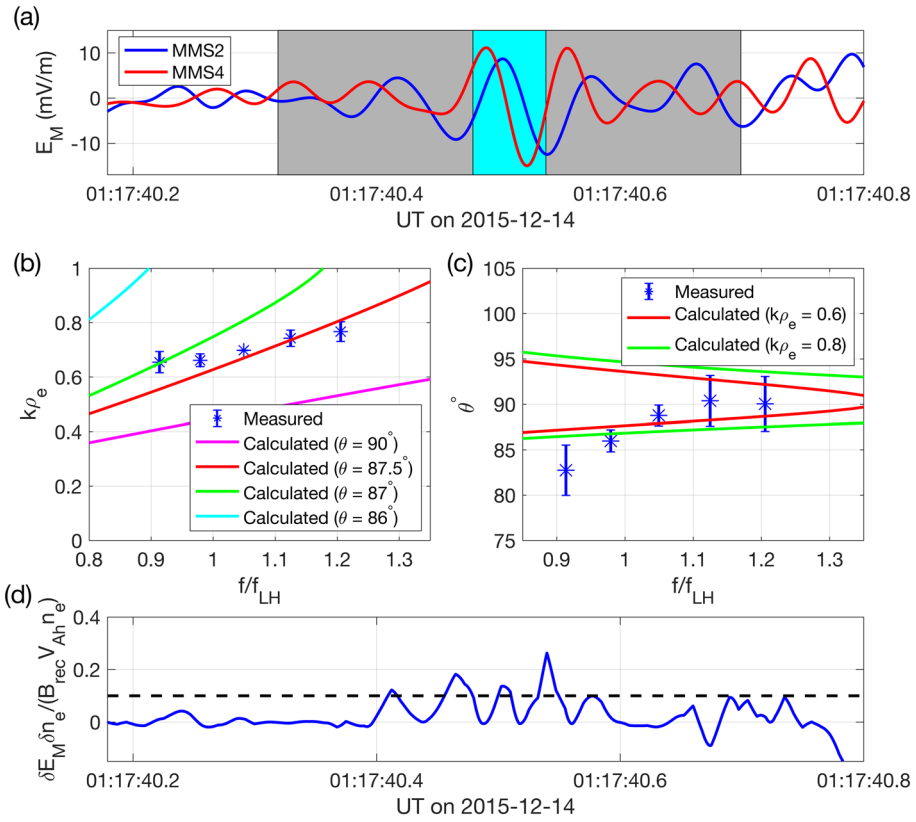

Figure 4. Wave vector measurement and comparison with the theory. (a) Profile of E_M near Region B, which is filtered by a low-pass filter with a cutoff frequency of 40 Hz. Signals from MMS2 and MMS4 correlate. The cyan box indicates the period where the analysis for the wave vector is performed. The gray box indicates the range of data used for the wavelet analysis. (b) Magnitude of the wave vector. Blue asterisks are measured values ($k\rho_e \sim 0.7$). Theoretical values with various θ are plotted with solid lines. (c) Angle between **k** and $\mathbf{B}_0$. Blue asterisks are values estimated by the SVD analysis. Theoretical values with various k are plotted with solid lines. The wave propagates almost perpendicular to $\mathbf{B}_0$. Error bars in (b) and (c) are from the standard deviation of the values computed during the period indicated by the cyan box in (a). Frequency values in (b) and (c) are the central frequency of the Morlet wavelet. (d) Anomalous drag by LHDW. $\delta E_M \delta n_e$ is normalized by $B_{rec} V_{Ah} n_e$. The black dashed line represents the nominal normalized reconnection rate for collisionless reconnection, 0.1 (Birn et al., 2001).

model. The measured $\hat{\mathbf{k}}$ has a dominant component along the x direction ($\hat{\mathbf{k}} = (0.987, -0.155, -0.019)$ for $f = 1.05 f_{LH}$), which supports the assumption of the negligible k_y. Error bars in Figures 4b and 4c are from the standard deviation of the values computed during the period indicated by the cyan box in Figure 4a.

The short-wavelength LHDW generates correlated fluctuations of the electron density and electric field, generating anomalous drag force between electrons and ions (Mozer et al., 2011). Figure 4d shows $\delta E_M \delta n_e$, normalized by $B_{rec} V_{Ah} \langle n_e \rangle$, where $V_{Ah} = 274$ km/s is the hybrid upstream Alfvén velocity for asymmetric reconnection (Cassak & Shay, 2007). Here, the angle bracket means the average of a quantity A from 01:17:40.2 to 01:17:40.8, and a fluctuating quantity is defined as $\delta A = A - \langle A \rangle$. Two fluctuating quantities δE_M and δn_e are correlated, producing a positive net value of $\delta E_M \delta n_e$, especially from 01:17:40.4 to 01:17:40.6. The value of $\delta E_M \delta n_e / \langle n_e \rangle$ over this period is significant, compared to the nominal reconnection rate for collisionless reconnection, $0.1 B_{rec} V_{Ah}$ (Birn et al., 2001), indicating a potential importance of the short-wavelength LHDW for electron and reconnection dynamics.

5. Summary and Discussions

In summary, we present LHDW activity inside a reconnecting current sheet measured by MMS with a moderate guide field. The long-wavelength LHDW exists inside the EDR where β_e is high, while the short-wavelength LHDW exists slightly outside the EDR where β_e is low. The analysis on the wave number **k** shows that **k** has a dominant perpendicular component with a magnitude of $k\rho_e \sim 0.7$ for $f \sim f_{LH}$, which

agrees with features of the fast-growing, short-wavelength LHDW (Davidson et al., 1977). For better understanding of LHDW, we have developed a local theoretical model for the dispersion relation. Results from this model explains the observed LHDW activity, including the magnitude and direction of **k**.

The model is based on the previous work in Ji et al. (2005) and has been improved to include the electron heat flux for better modeling of the perturbed parallel electron pressure, electron temperature anisotropy, parallel electron flow, and independent computation of the perturbed electron density for electrostatic effects. This model can calculate the dispersion with an arbitrary angle between the wave vector and magnetic field, unlike the kinetic treatment of LHDW (Davidson et al., 1977).

The limitation of this local model should be discussed. This analysis assumes no wave propagation along the gradient direction, neglecting the global structure of the current sheet. To address this issue, a global eigenmode analysis (Daughton, 2003; Tummel et al., 2014) should be carried out, which is our future work. For this event with a large current sheet width ($\sim d_i$, however, this local analysis seems acceptable, which makes the length scale along the y direction much larger than the wavelength.

This model assumes no temperature gradient for both electrons and ions, but the temperature gradient may be important for LHDW activity. With parameters measured in Region B, however, the results are not sensitive against relatively small change in the local temperature.

This study shows that the short-wavelength LHDW can exist in the EDR with a sufficient guide field, which is supported by recent observations (Chen et al., 2019). A strong guide field lowers the electron beta in the EDR, such that the short-wavelength LHDW can be the most unstable mode. Moreover, the short-wavelength LHDW induces fluctuations in the electric field and density that are correlate with each other, generating drag force between electrons and ions. It will be interesting to see how the short-wavelength LHDW can affect electron and reconnection dynamics in the EDR during reconnection with a high guide field. Further systematic research on this topic is warranted both in space (i.e., Chen et al., 2019) and in laboratory (i.e., Stechow et al., 2018).

Data Availability Statement

All MMS data used are available online (https://lasp.colorado.edu/mms/sdc/public/). Digital data used for all figures are available in the DataSpace of Princeton University (http://arks.princeton.edu/ark:/88435/dsp01x920g025r).

Acknowledgments
This work was supported by DOE Contract No. DE-AC0209CH11466, NASA grants NNH14AX63I and NNH15AB29I, NSF grants AGS-1552142, AGS-1619584, DOE grants DESC0016278, DE-FG02-04ER54746, NSF-DOE partnership in plasma science grant DE-FG02-00ER54585, and the NASA MMS mission.

References

Birn, J., Drake, J. F., Shay, M. A., Rogers, B. N., Denton, R. E., Hesse, M., et al. (2001). Geospace Environmental Modeling (GEM) magnetic reconnection challenge. *Journal of Geophysical Research*, *106*, 3715–3719. https://doi.org/10.1029/1999JA900449

Carter, T. A., Ji, H., Trintchouk, F., Yamada, M., & Kulsrud, R. M. (2001). Measurement of lower-hybrid drift turbulence in a reconnecting current sheet. *Physical Review Letters*, *88*, 15001. https://doi.org/10.1103/PhysRevLett.88.015001

Cassak, P. A., & Shay, M. A. (2007). Scaling of asymmetric magnetic reconnection: General theory and collisional simulations. *Physics of Plasmas*, *14*(10), 102114. https://doi.org/10.1063/1.2795630

Chen, L.-J., Hesse, M., Wang, S., Gershman, D., Ergun, R. E., Burch, J., et al. (2017). Electron diffusion region during magnetopause reconnection with an intermediate guide field: Magnetospheric multiscale observations. *Journal of Geophysical Research: Space Physics*, *122*, 5235–5246. https://doi.org/10.1002/2017JA024004

Chen, L.-J., Wang, S., Hesse, M., Ergun, R. E., Moore, T., Giles, B., et al. (2019). Electron diffusion regions in magnetotail reconnection under varying guide fields. *Geophysical Research Letters*, *46*, 6230–6238. https://doi.org/10.1029/2019GL082393

Daughton, W. (2003). Electromagnetic properties of the lower-hybrid drift instability in a thin current sheet. *Physics of Plasmas*, *10*(8), 3103–3119. https://doi.org/10.1063/1.1594724

Davidson, R., Gladd, N., Wu, C., & Huba, J. (1977). Effects of finite plasma beta on the lower-hybrid drift instability. *Physics of Fluids*, *20*, 301.

Ergun, R. E., Chen, L.-J., Wilder, F. D., Ahmadi, N., Eriksson, S., Usanova, M. E., et al. (2017). Drift waves, intense parallel electric fields, and turbulence associated with asymmetric magnetic reconnection at the magnetopause. *Geophysical Research Letters*, *44*, 2978–2986. https://doi.org/10.1002/2016GL072493

Ergun, R. E., Tucker, S., Westfall, J., Goodrich, K. A., Malaspina, D. M., Summers, D., et al. (2016). The axial double probe and fields signal processing for the MMS mission. *Space Science Reviews*, *199*(1), 167–188. https://doi.org/10.1007/s11214-014-0115-x

Fox, W., Sciortino, F., Stechow, A. V., Jara-Almonte, J., Yoo, J., Ji, H., & Yamada, M. (2017). Experimental verification of the role of electron pressure in fast magnetic reconnection with a guide field. *Physical Review Letters*, *118*, 125002. https://doi.org/10.1103/PhysRevLett.118.125002

Graham, D. B., Khotyaintsev, Y. V., Norgren, C., Vaivads, A., Andr, M., Toledo-Redondo, S., et al. (2017). Lower hybrid waves in the ion diffusion and magnetospheric inflow regions. *Journal of Geophysical Research: Space Physics*, *122*, 517–533. https://doi.org/10.1002/2016JA023572

Haaland, S. E., Sonnerup, B. U. Ö., Dunlop, M. W., Balogh, A., Georgescu, E., Hasegawa, H., et al. (2004). Four-spacecraft determination of magnetopause orientation, motion and thickness: Comparison with results from single-spacecraft methods. *Annales Geophysicae*, *22*(4), 1347–1365. https://doi.org/10.5194/angeo-22-1347-2004

Ji, J.-Y., & Joseph, I. (2018). Electron parallel closures for the 3 + 1 fluid model. *Physics of Plasmas*, *25*(3), 32117. https://doi.org/10.1063/1.5014996

Ji, H., Kulsrud, R., Fox, W., & Yamada, M. (2005). An obliquely propagating electromagnetic drift instability in the lower hybrid frequency range. *Journal of Geophysical Research*, *110*, A08212. https://doi.org/10.1029/2005JA011188

Ji, H., Terry, S., Yamada, M., Kulsrud, R., Kuritsyn, A., & Ren, Y. (2004). Electromagnetic fluctuations during fast reconnection in a laboratory plasma. *Physical Review Letters*, *92*, 115001. https://doi.org/10.1103/PhysRevLett.92.115001

Le Contel, O., Leroy, P., Roux, A., Coillot, C., Alison, D., Bouabdellah, A., et al. (2016). The search-coil magnetometer for MMS. *Space Science Reviews*, *199*(1), 257–282. https://doi.org/10.1007/s11214-014-0096-9

Lindqvist, P.-A., Olsson, G., Torbert, R. B., King, B., Granoff, M., Rau, D., et al. (2016). The spin-plane double probe electric field instrument for MMS. *Space Science Reviews*, *199*(1), 137–165. https://doi.org/10.1007/s11214-014-0116-9

Mozer, F. S., Angelopoulos, V., Bonnell, J., Glassmeier, K. H., & McFadden, J. P. (2008). THEMIS observations of modified Hall fields in asymmetric magnetic field reconnection. *Geophysical Research Letters*, *35*, L17S04. https://doi.org/10.1029/2007GL033033

Mozer, F. S., Wilber, M., & Drake, J. F. (2011). Wave associated anomalous drag during magnetic field reconnection. *Physics of Plasmas*, *18*(10), 102902. https://doi.org/10.1063/1.3647508

Norgren, C., Vaivads, A., Khotyaintsev, Y. V., & André, M. (2012). Lower hybrid drift waves: Space observations. *Physical Review Letters*, *109*, 055001. https://doi.org/10.1103/PhysRevLett.109.055001

Pollock, C., Moore, T., Jacques, A., Burch, J., Gliese, U., Saito, Y., et al. (2016). Fast plasma investigation for magnetospheric multiscale. *Space Science Reviews*, *199*(1), 331–406. https://doi.org/10.1007/s11214-016-0245-4

Pritchett, P. L. (2008). Collisionless magnetic reconnection in an asymmetric current sheet. *Journal of Geophysical Research*, *113*, A06210. https://doi.org/10.1029/2007JA012930

Pritchett, P. L., & Coroniti, F. V. (2004). Three-dimensional collisionless magnetic reconnection in the presence of a guide field. *Journal of Geophysical Research*, *109*, A01220. https://doi.org/10.1029/2003JA009999

Ricci, P., Blackbill, J., Daughton, W., & Lapenta, G. (2004). Influence of the lower hybrid drift instability on the onset of magnetic reconnection. *Physics of Plasmas*, *11*, 4489.

Roytershteyn, V., Daughton, W., Karimabadi, H., & Mozer, F. S. (2012). Influence of the lower-hybrid drift instability on magnetic reconnection in asymmetric configurations. *Physical Review Letters*, *108*, 185001. https://doi.org/10.1103/PhysRevLett.108.185001

Roytershteyn, V., Dorfman, S., Daughton, W., Ji, H., Yamada, M., & Karimabadi, H. (2013). Electromagnetic instability of thin reconnection layers: Comparison of three-dimensional simulations with MRX observations. *Physics of Plasmas*, *20*(6), 061212. https://doi.org/10.1063/1.4811371

Russell, C. T., Anderson, B. J., Baumjohann, W., Bromund, K. R., Dearborn, D., Fischer, D., et al. (2016). The magnetospheric multiscale magnetometers. *Space Science Reviews*, *199*(1), 189–256. https://doi.org/10.1007/s11214-014-0057-3

Santolík, O., Parrot, M., & Lefeuvre, F. (2003). Singular value decomposition methods for wave propagation analysis. *Radio Science*, *38*(1), 1010. https://doi.org/10.1029/2000RS002523

Stechow, A. V., Fox, W., Jara-Almonte, J., Yoo, J., Ji, H., & Yamada, M. (2018). Electromagnetic fluctuations during guide field reconnection in a laboratory plasma. *Physics of Plasmas*, *25*(5), 52120. https://doi.org/10.1063/1.5025827

Tharp, T. D., Yamada, M., Ji, H., Lawrence, E., Dorfman, S., Myers, C. E., & Yoo, J. (2012). Quantitative study of guide-field effects on hall reconnection in a laboratory plasma. *Physical Review Letters*, *109*, 165002. https://doi.org/10.1103/PhysRevLett.109.165002

Torrence, C., & Compo, G. P. (1998). A practical guide to wavelet analysis. *Bulletin of the American Meteorological Society*, *79*(1), 61–78. https://doi.org/10.1175/1520-0477(1998)079<0061:APGTWA>2.0.CO;2

Tummel, K., Chen, L., Wang, Z., Wang, X. Y., & Lin, Y. (2014). Gyrokinetic theory of electrostatic lower-hybrid drift instabilities in a current sheet with guide field. *Physics of Plasmas*, *21*(5), 52104. https://doi.org/10.1063/1.4875720

Yamada, M., Kulsrud, R., & Ji, H. (2010). Magnetic reconnection. *Reviews of Modern Physics*, *82*, 603–664. https://doi.org/10.1103/RevModPhys.82.603

Yoo, J., Jara-Almonte, J., Yerger, E., Wang, S., Qian, T., Le, A., et al. (2018). Whistler wave generation by anisotropic tail electrons during asymmetric magnetic reconnection in space and laboratory. *Geophysical Research Letters*, *45*, 8054–8061. https://doi.org/10.1029/2018GL079278

Yoo, J., Wang, S., Yerger, E., Jara-Almonte, J., Ji, H., Yamada, M., et al. (2019). Whistler wave generation by electron temperature anisotropy during magnetic reconnection at the magnetopause. *Physics of Plasmas*, *26*(5), 52902. https://doi.org/10.1063/1.5094636

Yoo, J., & Yamada, M. (2012). Experimental evaluation of common spacecraft data analysis techniques for reconnection region analysis in a laboratory plasma. *Journal of Geophysical Research*, *117*, A12202. https://doi.org/10.1029/2012JA017742

Yoo, J., Yamada, M., Ji, H., Jara-Almonte, J., & Myers, C. E. (2014). Bulk ion acceleration and particle heating during magnetic reconnection in a laboratory plasma. *Physics of Plasmas*, *21*(5), 55706. https://doi.org/10.1063/1.4874331

Yoo, J., Yamada, M., Ji, H., Jara-Almonte, J., Myers, C. E., & Chen, L.-J. (2014). Laboratory study of magnetic reconnection with a density asymmetry across the current sheet. *Physical Review Letters*, *113*, 095002. https://doi.org/10.1103/PhysRevLett.113.095002